



HAL
open science

SOFIA/EXES observations of warm H₂ at high spectral resolution: II. IC443C, NGC2071, and 3C391

David Neufeld, Curtis Dewitt, Pierre Lesaffre, Sylvie Cabrit, Antoine Gusdorf,
Le Ngoc Tram, William Reach

► To cite this version:

David Neufeld, Curtis Dewitt, Pierre Lesaffre, Sylvie Cabrit, Antoine Gusdorf, et al.. SOFIA/EXES observations of warm H₂ at high spectral resolution: II. IC443C, NGC2071, and 3C391. *The Astrophysical Journal*, 2024, 976 (1), pp.3. 10.3847/1538-4357/ad83b7 . hal-04780116

HAL Id: hal-04780116

<https://hal.science/hal-04780116v1>

Submitted on 21 Jan 2025

HAL is a multi-disciplinary open access archive for the deposit and dissemination of scientific research documents, whether they are published or not. The documents may come from teaching and research institutions in France or abroad, or from public or private research centers.



L'archive ouverte pluridisciplinaire **HAL**, est destinée au dépôt et à la diffusion de documents scientifiques de niveau recherche, publiés ou non, émanant des établissements d'enseignement et de recherche français ou étrangers, des laboratoires publics ou privés.



Distributed under a Creative Commons Attribution 4.0 International License



SOFIA/EXES Observations of Warm H₂ at High Spectral Resolution. II. IC 443C, NGC 2071, and 3C 391

David A. Neufeld^{1,6} , Curtis DeWitt², Pierre Lesaffre^{3,4}, Sylvie Cabrit⁴, Antoine Gusdorf^{3,4}, Le Ngoc Tram⁵, and William T. Reach² 

¹ Department of Physics & Astronomy, Johns Hopkins Univ., Baltimore, MD 21218, USA; neufeld@pha.jhu.edu

² Space Science Institute, 4765 Walnut Street, Suite 205, Boulder, CO 80301, USA

³ Laboratoire de Physique de l'École Normale Supérieure, ENS, Université PSL, CNRS, Sorbonne Université, Université Paris Cité, F-75005, Paris, France

⁴ Observatoire de Paris, PSL University, Sorbonne Université, LERMA, 75014, Paris, France

⁵ Max-Planck-Institut für Radioastronomie, Auf dem Hügel 69, D-53121, Bonn, Germany

Received 2024 August 5; revised 2024 October 3; accepted 2024 October 3; published 2024 November 11

Abstract

Using the EXES instrument on SOFIA, we have obtained velocity-resolved spectra of several pure rotational lines of H₂ toward shocked molecular gas within three Galactic sources: the supernova remnant (SNR) IC 443 (clump C), a protostellar outflow in the intermediate-mass star-forming region NGC 2071, and the SNR 3C 391. These observations had the goal of searching for expected velocity shifts between ortho- and para-H₂ transitions emitted by C-type shocks. In contrast in our previous similar study of HH7, the result of our search was negative: no velocity shifts were reliably detected. Several possible explanations for the absence of such shifts are discussed: these include a preshock ortho-to-para ratio that is already close to the high-temperature equilibrium value of 3 (in the case of IC 443C), the more complex shock structures evident in all these sources, and the larger projected aperture sizes relative to those in the observations of HH7.

Unified Astronomy Thesaurus concepts: [Shocks \(2086\)](#); [Interstellar molecules \(849\)](#); [Infrared astronomy \(786\)](#); [Supernova remnants \(1667\)](#)

1. Introduction

Previous observations of shocked interstellar gas, performed with SOFIA/EXES toward the classic bow shock in HH7 (D. A. Neufeld et al. 2019, hereafter N19), have provided key constraints on shock physics through velocity-resolved measurements of H₂ rotational line profiles. These revealed, for the first time, clear velocity shifts, in the range 3–4 km s^{−1}, between emission lines of ortho-H₂ (the S(5) and S(7) transitions) and those of para-H₂ (the S(4) and S(6) transitions). As discussed by N19, to which the reader is referred for a more extensive discussion, these shifts are naturally explained as resulting from the relative slow conversion of para-H₂ to ortho-H₂ within the region of elevated gas temperature within an interstellar shock; as such, they provide perhaps the most direct evidence for “C-type” shocks in which the flow velocity varies continuously within the warm shocked gas thanks to ion-neutral collisions in the magnetized medium (B. T. Draine 1980; D. F. Chernoff et al. 1982; D. R. Flower et al. 1985). Within the velocity range covered by the emission line, the ortho-to-para ratio (OPR; the determination of which is discussed in Section 4 below) was found to vary smoothly between ∼0.5 and 2.0 across the line profile, in good agreement with the predictions of C-type shock models in which cold ambient gas, with a low initial OPR, is accelerated and heated; this is accompanied by partial para-H₂ to ortho-H₂ conversion toward the equilibrium OPR of 3 expected in warm gas.

Motivated by this earlier result, we have observed the S(4)–S(7) rotational lines of H₂ with SOFIA/EXES toward three additional sources where shock-heated gas is present. These were chosen to reflect a diversity of interstellar shock types, all rather different from that in HH7, and comprise the supernova remnants (SNR) IC 443 (clump C) and 3C 391, along with a protostellar outflow in the intermediate-mass star-forming region NGC 2071. All three sources had been observed with the Spitzer Space Telescope, which obtained spectral line maps for the S(0)–S(7) H₂ rotational lines (D. A. Neufeld et al. 2007, 2009). Full descriptions of these sources were given in those earlier publications and will not be repeated here. At the spectral resolving power of Spitzer Infrared Spectrometer (IRS), $\lambda/\Delta\lambda = 60$ for the S(3)–S(7) lines and $\lambda/\Delta\lambda = 600$ for the S(0)–S(2) lines, the H₂ rotational line profiles could not be measured; moreover, because of the limited spectral resolution, the S(6) line could not be observed reliably toward 3C 391 because of a strong polycyclic aromatic hydrocarbon emission feature around 6.2 μm .

As in several other shocked sources observed with Spitzer, the H₂ rotational diagrams observed toward all three sources could be fit successfully with a two-component model that invoked a warm (250–350 K) gas component, responsible for the lower-lying transitions, and a hot (1000–1100 K) component, responsible for the higher-lying transitions. Such models yield best estimates of 0.52 and 0.65 for the OPR in the warm components in NGC 2071 and 3C 391, respectively, far lower than the value ∼3 expected in equilibrium at the measured gas temperature; the low H₂ OPRs measured for the warm gas in these sources are clearly a relic of an earlier epoch when the gas had reached equilibrium at a lower temperature. In the absence of flux measurement for the S(6) line, an OPR could not be obtained for the hot gas component in 3C 391, while that observed for the hot component in NGC 2071 was consistent

⁶ Author to whom any correspondence should be addressed.



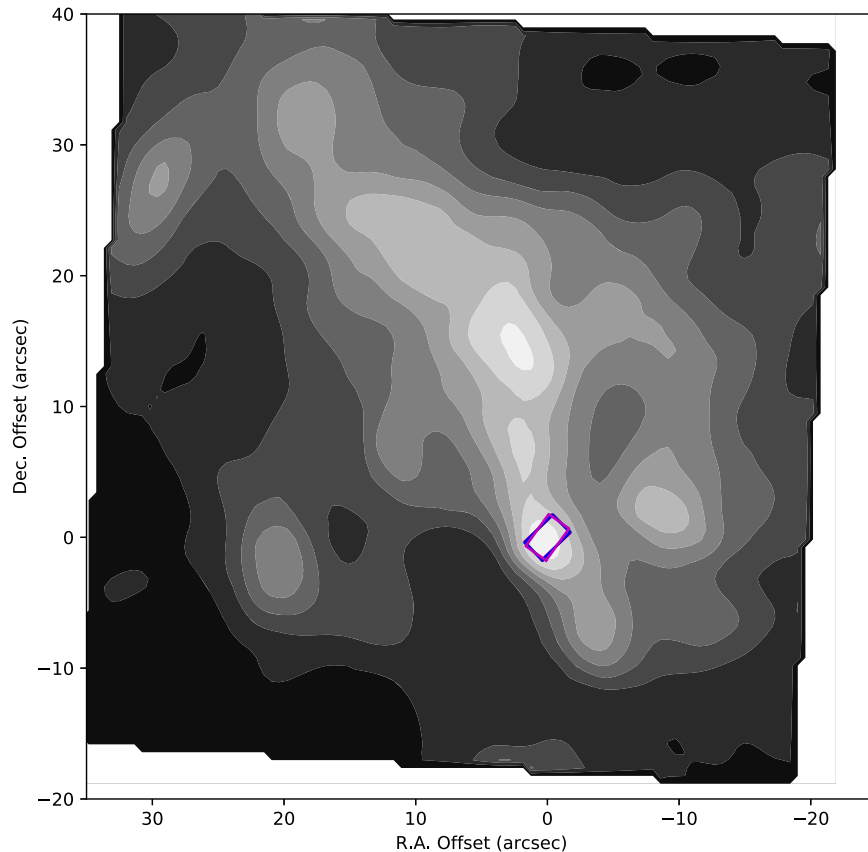


Figure 1. Slit positions for IC 443C. Grayscale: map of H₂ S(5) intensity from Spitzer/IRS (D. A. Neufeld et al. 2007). Colored rectangles: location and orientation of the extracted apertures for SOFIA/EXES observations of H₂ S(4) (red), S(5) (green), S(6) (blue), and S(7) (magenta).

with 3. For IC 443C, by contrast, the S(0)–S(7) line ratios were entirely consistent with an equilibrium OPR of 3 for *both* the warm and hot components. These Spitzer observations suggested that NGC 2071 and 3C 391 were good candidates for the detection of ortho–para line shifts like those measured toward HH7. IC 443C, on the other hand, was selected as a control in which no such shifts were expected.

In Section 2 below, we describe the observations and data reduction. The resultant spectra are presented in Section 3. They are discussed in Section 4, where the gas temperature and OPR is determined as a function of velocity along the line of sight.

2. Observations and Data Reduction

We observed the S(4), S(5), S(6), and S(7) pure rotational transitions of H₂ toward a single position in each of IC 443C, 3C 391, and NGC 2071. In each case, to maximize the observed signal, the EXES slit was centered at the peak of the H₂ S(5) emission, as revealed by the previous line mapping observations with Spitzer/IRS and without regard to the OPR ratio. Although the IRS spectrometer lacked the spectral resolution to resolve the H₂ line profiles, it allowed maps of size $\sim 1' \times 1'$ to be constructed by scanning the spectrometer slit perpendicular to its length. In Figures 1–3, we show for each source the location and position angle of the EXES slit on the Spitzer maps of the H₂ S(5) intensity. The observing parameters are given in Table 1, along with the wavelength and upper state energy for each line (E. Roueff et al. 2019).

The observations were performed with a slit width of $1''.9$, using the EXES instrument (M. J. Richter et al. 2018) in

high-medium mode, a configuration that provides a spectral resolving power $\lambda/\Delta\lambda$ of 86,000 ($\Delta v = 3.5 \text{ km s}^{-1}$). In Table 1, we list for each spectral line and each source the rest wavelength, slit center position, date(s) of observation, integration time, and range of slit position angles (degrees east of north) during the course of the observation. To enable the subtraction of telluric emission features, the telescope was nodded periodically to a reference position devoid of H₂ emission.

The data were reduced using the Redux pipeline (M. Clarke et al. 2015) with the fspextool software package—a modification of the Spextool package (M. C. Cushing et al. 2004)—which performs wavelength calibration. The latter was obtained from observations of multiple atmospheric lines of water and methane within each bandpass: we conservatively estimate its accuracy as 0.3 km s^{-1} . The absolute flux calibration is accurate to $\sim 25\%$ and the relative flux calibration to $\sim 12.5\%$. The atmospheric transmission is expected to exceed 90% for all observed transitions, with the exception of the S(4) line observations toward 3C 391. Because of the unfavorable radial velocity of the source at the time of those observations, they were severely affected by telluric methane lines and could not be used.

All the observations of a given source were conducted within a time period of ~ 3 months or less. This is much smaller than the minimum expected variability timescale for a source at a distance d : $\tau = (\theta/\text{rad})d/v_t = 36(d/400 \text{ pc})(100 \text{ km s}^{-1}/v_t) \text{ yr}$, where $\theta = 1''.9$ is the slit width and v_t is the transverse velocity of the source.

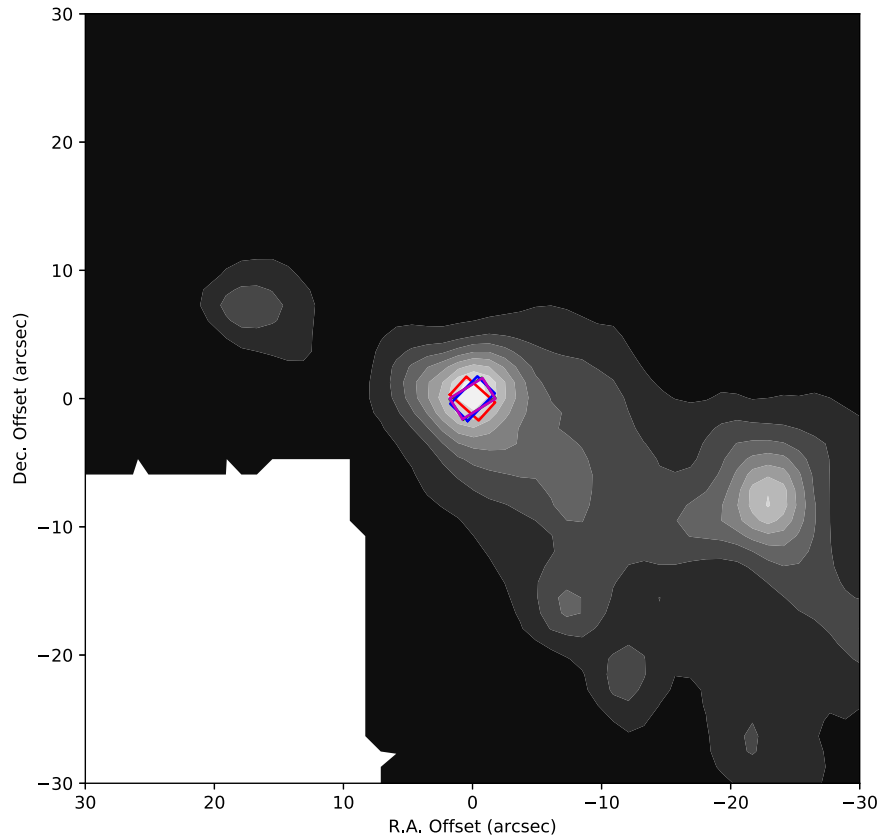


Figure 2. Slit positions for NGC 2071. Grayscale: map of H_2 S(5) intensity from Spitzer/IRS (D. A. Neufeld et al. 2009). Colored rectangles: location and orientation of the extracted apertures for SOFIA/EXES observations of H_2 S(4) (red), S(5) (green), S(6) (blue), and S(7) (magenta).

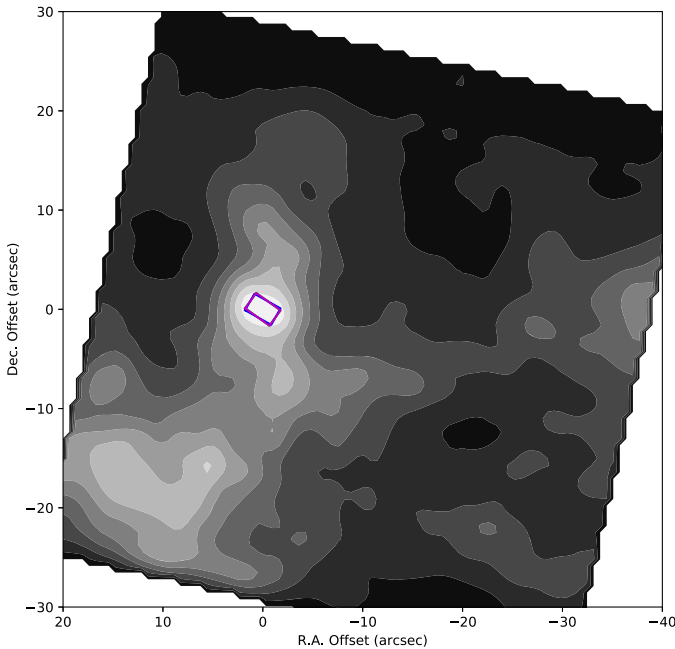


Figure 3. Slit positions for 3C 391. Grayscale: map of H_2 S(5) intensity from Spitzer/IRS (D. A. Neufeld et al. 2007). Colored rectangles: location and orientation of the extracted apertures for SOFIA/EXES observations of S(5) (green), S(6) (blue), and S(7) (magenta).

3. Results

With the exception of the S(4) line toward 3C 391, all four transitions were securely detected toward each target source.

The resultant spectra are shown in Figures 4–6. Where multiple observations were performed, the spectra were reduced individually and then coadded with a weighting proportional to the exposure time. Where the spectra obtained by N19 toward HH7 could be adequately fitted with a single Gaussian feature, two Gaussian components are needed to fit the lines detected in the present study. Solid lines show the two-component fits to the observed spectra: these use the Levenberg–Marquardt algorithm to fit two Gaussians and a first-order baseline to the data. The velocity centroids, line widths (FWHM), and peak line intensities for those components are presented in Table 2, along with the standard errors on each parameter. We note that these standard errors are simply statistical in nature, and do not include uncertainties associated with flux and wavelength calibration (see Section 2 above). Moreover, particularly for broad components, additional errors may result from baseline ripple (i.e., departures of the baseline from the linear function assumed here). Vertical black lines in Figures 4–6 indicate the velocity centroids for the Gaussian components, with horizontal bars at the bottom indicating the standard errors (i.e., 68% confidence limits not accounting for systematic uncertainties).

Perhaps by coincidence, IC 443C and NGC 2071 show rather similar spectra. Each exhibits a narrow component—of best-fit FWHM $\sim 12 \text{ km s}^{-1}$ for the strongest, best-observed lines (i.e., S(4) and S(5))—and a broader component of smaller peak intensity that is blueshifted $\sim 20 \text{ km s}^{-1}$ relative to the narrow component. The observed line profile for the S(5) line in IC 443C has been previously modeled by W. T. Reach et al. (2019), who found that most of the emission could be accounted for by a combination of nonstationary CJ-type

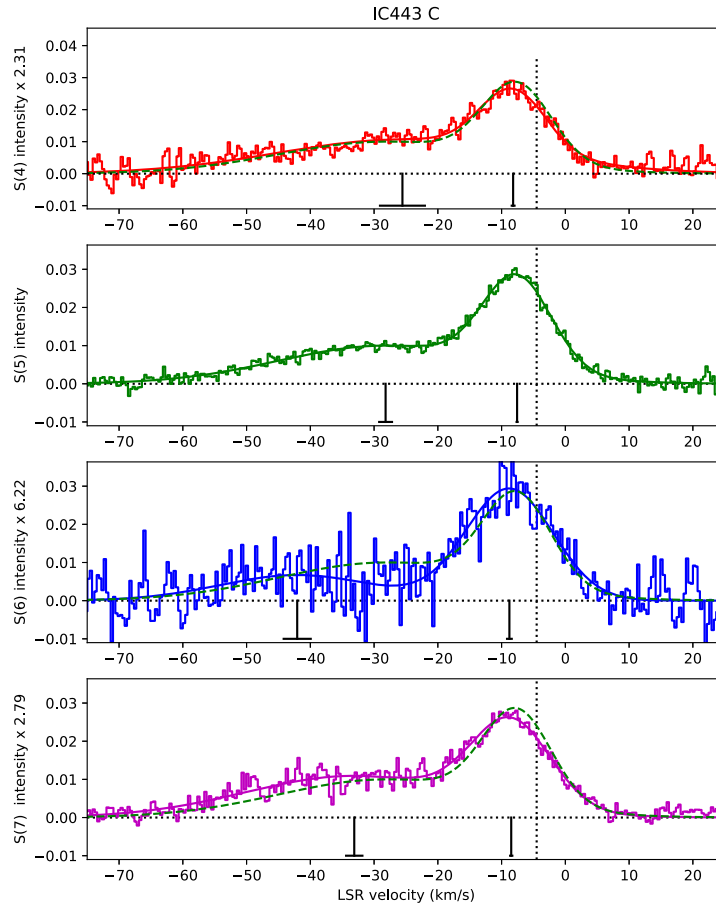


Figure 4. Spectra obtained toward IC 443C. The average intensity within the $1''.9 \times 3''.0$ extraction region is plotted in units of $\text{erg cm}^{-2} \text{s}^{-1} \text{sr}^{-1} / \text{cm}^{-1}$. Solid curves show the two-Gaussian fits to each line. The dotted green lines show the H₂ S(5) line profile, scaled and overplotted in the other panels for comparison. Vertical black lines indicate the velocity centroids for the Gaussian components, with horizontal bars at the bottom indicating the standard errors. The LSR velocity of the source is indicated by the dotted black vertical line.

Table 1
Observational Details

Line	H ₂ S(4)	H ₂ S(5)	H ₂ S(6)	H ₂ S(7)
Symmetry	$J = 6-4$ para	$J = 7-5$ ortho	$J = 8-6$ para	$J = 9-7$ ortho
Rest wavelength (μm)	8.0250410	6.9095086	6.1085638	5.5111833
Upper state energy (E_U/k in K)	3474.5	4586.1	5829.8	7196.7
Observations of IC 443C with the slit centered at $6^{\text{h}}17^{\text{m}}42^{\text{s}}.37$ $22^{\circ}21'16''.9$ (J2000)				
Date (UT)	2022 Feb 25 2022 Mar 9	2022 Feb 25	2022 Mar 1	2022 Mar 7
Integration time ^a (s)	1216 1088	1024	1920	2560
Slit position angle ^b	311.9–309.4 310.6–307.1	317.0–315.6	314.7–309.7	324.3–315.9
Observations of NGC 2071 with the slit centered at $5^{\text{h}}47^{\text{m}}08^{\text{s}}.21$ $0^{\circ}22'52''.7$ (J2000)				
Date (UT)	2021 Dec 2 2021 Dec 4	2021 Dec 1 2021 Dec 2	2022 Mar 5	2022 Feb 6
Integration time ^a (s)	1024 2048	768 512	1280	1280
Slit position angle ^b	248.5–248.5 227.9–227.9	303.7–302.8 248.5–248.5	315.5–316.2	301.9–304.8
Observations of 3C 391 with the slit centered at $18^{\text{h}}49^{\text{m}}22^{\text{s}}.56$ $-0^{\circ}57'17''.2$ (J2000)				
Date (UT)		2022 Mar 8	2022 Mar 9	2022 Feb 24 2022 Mar 9
Integration time ^a (s)		1664	2240	1920 1280
Slit position angle ^b		234.0–233.2	240.6–240.6	234.6–234.1 243.1–240.6

Notes.

^a Detector integration times, on source.

^b Degrees east of north.

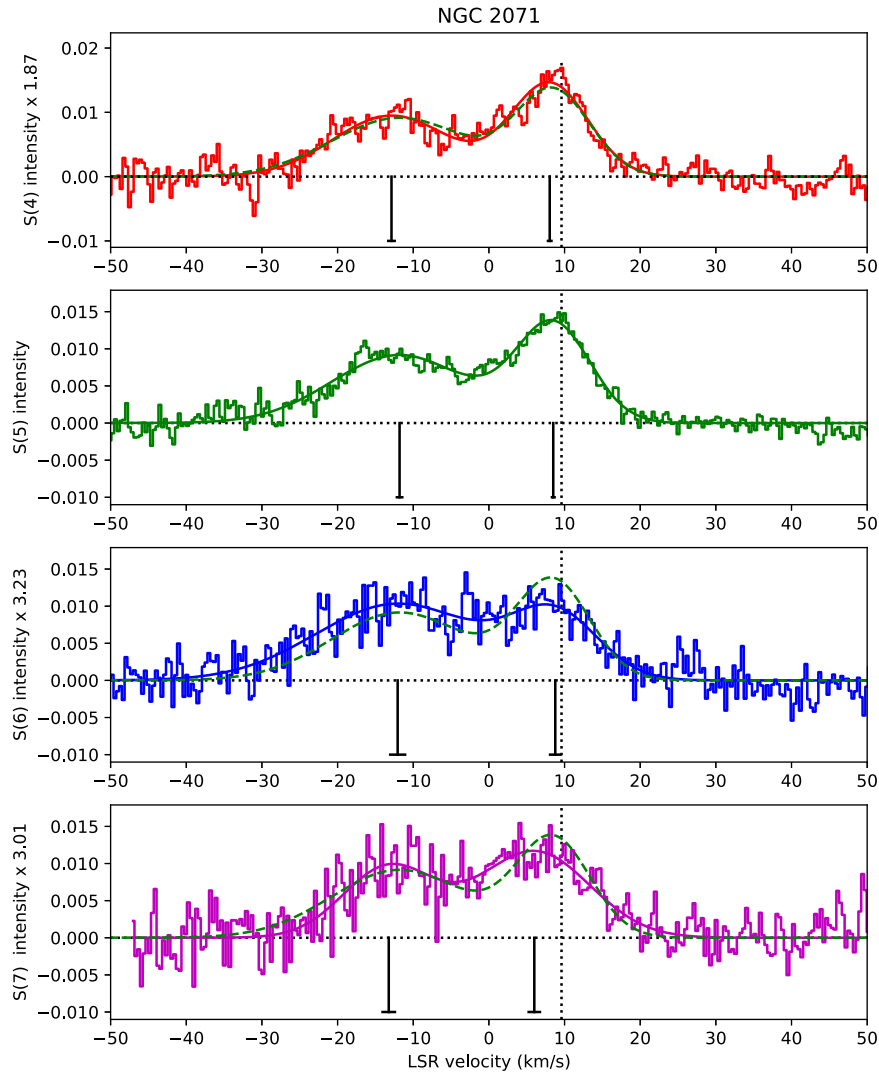


Figure 5. Same as Figure 4, but for NGC 2071

shocks consistent with the SNR expansion ram pressure (one at 60 km s^{-1} propagating in a 2000 cm^{-3} clump producing the broad component, and one at 37 km s^{-1} propagating in a 6000 cm^{-3} producing the narrower component, both viewed close to face-on.)

The line emission from 3C 391 is weaker and the observed spectrum is less well-determined, although also similar to those in IC 443C and NGC 2071. The narrow components in IC 443C and NGC 2071 present the best opportunity to detect a systematic velocity shift between the ortho- H_2 (S(5) and S(7)) para- H_2 (S(4) and S(6)) lines, but none is observed reliably. The shift between the best-fit velocity centroids for the S(4) and S(5) lines is only 0.6 ± 0.2 and $0.5 \pm 0.3 \text{ km s}^{-1}$, respectively, for the narrow components in IC 443C and NGC 2071. These values are, at best, of marginal statistical significance—even neglecting possible systematic uncertainties—and are far smaller than the $3\text{--}4 \text{ km s}^{-1}$ shift discovered (N19) in HH7. A caveat applies to the comparison between the S(4) and S(5) line profiles in NGC 2071, because the slit position angles are significantly different for the S(4) line observation and the second S(5) observation (accounting for 40% of the S(5) observing time). Any systematic difference this might lead to is

mitigated by the fact that the $1''.9 \times 3''.0$ extraction region is only modestly elongated with an aspect ratio of 1.58.

4. Discussion

Because the quadrupole H_2 rotational lines are always optically thin, the intensity of the S(X-2) line is linearly proportional to the column density in the upper $J = X$ state. Following N19, we may conveniently define excitation temperatures, T_{XY} , that characterize the column density ratios measured between pairs of states $J = X$ and $J = Y$ of the same spin symmetry (i.e., with X and Y both odd or both even). And given a triad of measured column densities for three consecutive J -states, X , Y , and Z , we may define the ortho-to-para, OPR_{XYZ} , that is needed to account for the $J = Y$ level population based on a linear interpolation of the rotational diagram between $J = X$ and $J = Z$. The results for the four parameters T_{86} , T_{97} , OPR_{678} , and OPR_{789} are shown in Figures 7–9 (crosses) in local standard of rest (LSR) velocity bins of width 2 km s^{-1} , along with a normalized plot showing the rebinned spectra. For each parameter, the average values are indicated both with text and a dashed colored line. The individual points have error bars that reflect the noise in the

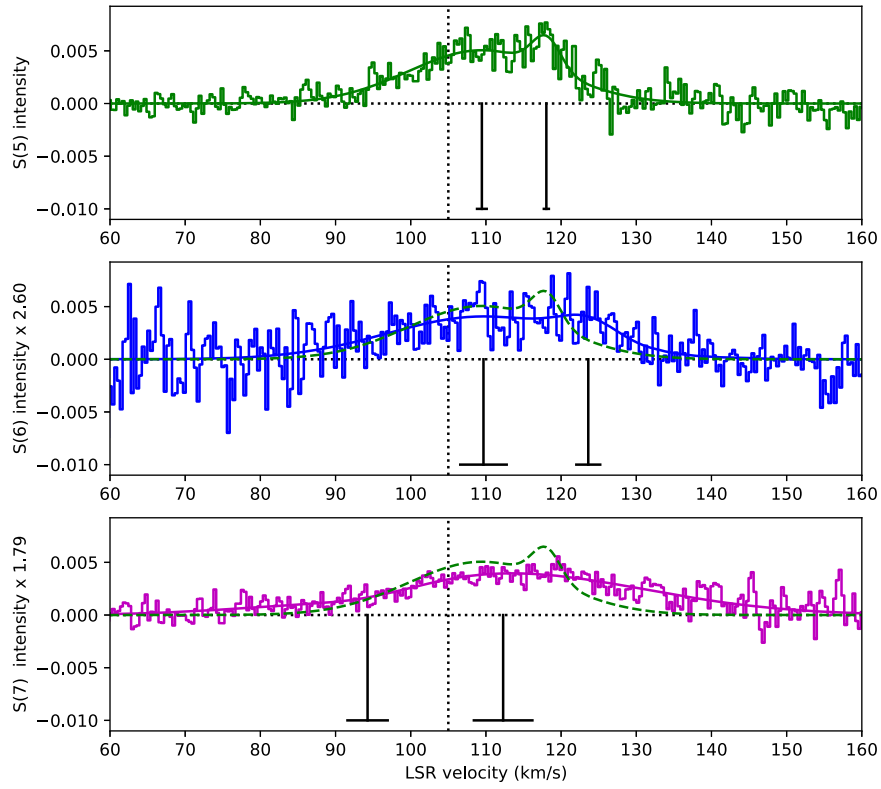


Figure 6. Same as Figure 4, but for 3C 391.

Table 2
Line Fit Parameters

Results for IC443 C				
Line	S(4)	S(5)	S(6)	S(7)
$\lambda_{\text{rest}} (\mu\text{m})$	8.02504108	6.90950858	6.10856384	5.511183259
$v_1 (\text{km s}^{-1})$	-8.2 ± 0.2	-7.6 ± 0.1	-8.8 ± 0.4	-8.5 ± 0.2
$\Delta v_1 (\text{km s}^{-1} \text{ FWHM})$	12.1 ± 0.9	12.6 ± 0.3	16.1 ± 1.0	14.6 ± 0.6
f_1^a	8.3 ± 0.6	24.0 ± 0.6	4.7 ± 0.2	8.0 ± 0.3
$v_2 (\text{km s}^{-1})$	-25.6 ± 3.5	-28.2 ± 1.0	-42.1 ± 2.1	-33.1 ± 1.3
$\Delta v_2 (\text{km s}^{-1} \text{ FWHM})$	46.3 ± 8.4	39.4 ± 2.5	28.7 ± 6.8	40.2 ± 3.9
f_2^a	4.6 ± 0.7	10.0 ± 0.3	1.1 ± 0.2	3.9 ± 0.2
Results for NGC 2071				
Line	S(4)	S(5)	S(6)	S(7)
$\lambda_{\text{rest}} (\mu\text{m})$	8.02504108	6.90950858	6.10856384	5.511183259
$v_1 (\text{km s}^{-1})$	8.0 ± 0.2	8.5 ± 0.2	8.8 ± 0.7	6.0 ± 0.7
$\Delta v_1 (\text{km s}^{-1} \text{ FWHM})$	12.0 ± 0.6	11.5 ± 0.4	13.5 ± 1.5	17.3 ± 1.8
f_1^a	7.7 ± 0.2	13.1 ± 0.3	2.6 ± 0.3	3.9 ± 0.2
$v_2 (\text{km s}^{-1})$	-12.9 ± 0.4	-11.8 ± 0.4	-12.1 ± 1.0	-13.2 ± 0.8
$\Delta v_2 (\text{km s}^{-1} \text{ FWHM})$	18.2 ± 1.2	21.2 ± 1.0	25.4 ± 2.6	14.2 ± 1.8
f_2^a	5.1 ± 0.2	9.2 ± 0.2	3.2 ± 0.1	3.2 ± 0.2
Results for 3C 391				
Line	S(4)	S(5)	S(6)	S(7)
$\lambda_{\text{rest}} (\mu\text{m})$	8.02504108	6.90950858	6.10856384	5.511183259
$v_1 (\text{km s}^{-1})$	N/A	118.0 ± 0.3	123.6 ± 1.6	112.3 ± 3.9
$\Delta v_1 (\text{km s}^{-1} \text{ FWHM})$	N/A	4.5 ± 0.9	9.2 ± 5.7	44.5 ± 7.6
f_1^a	N/A	3.0 ± 0.5	0.7 ± 0.4	2.2 ± 0.3
$v_2 (\text{km s}^{-1})$	N/A	109.5 ± 0.6	109.7 ± 3.1	94.3 ± 2.7
$\Delta v_2 (\text{km s}^{-1} \text{ FWHM})$	N/A	23.0 ± 1.3	30.0 ± 6.1	18.1 ± 11.7
f_2^a	N/A	5.1 ± 0.2	1.6 ± 0.2	-0.5 ± 0.5

Note.

^a Units of $10^{-3} \text{ erg cm}^{-2} \text{ s}^{-1} \text{ sr}^{-1} / \text{cm}^{-1}$, where $10^{-3} \text{ erg cm}^{-2} \text{ s}^{-1} \text{ sr}^{-1} / \text{cm}^{-1} = 3335.64 \text{ MJy sr}^{-1}$.

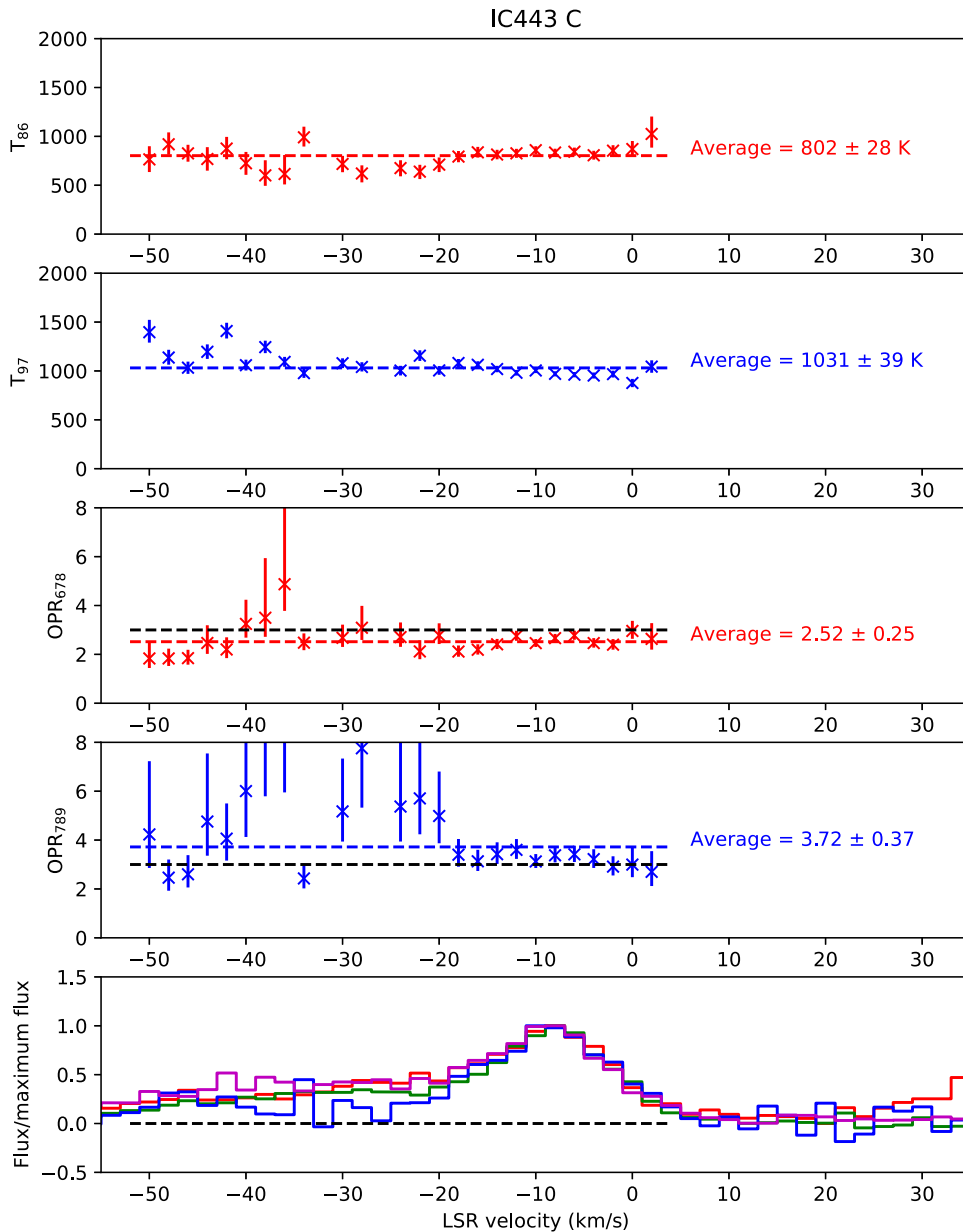


Figure 7. Results obtained for IC 443C. Top two panels: T_{XY} , the temperature derived from the relative populations in the H_2 $J = X$ and Y states. Next two panels: OPR_{XYZ} , the ortho-to-para ratio derived from the relative populations in the H_2 $J = X$, Y , and Z states. Bottom panels: scaled spectra, rebinned to 2 km s^{-1} resolution, with the same color coding as in Figures 4–6.

spectrum but not the flux calibration uncertainties; here, the rms noise was propagated with a Monte Carlo method. The average values indicated with text, by contrast, *do* include the systematic uncertainties associated with flux calibration (see Section 2 above). Dashed black lines indicate the values (both 3.00) that OPR_{678} and OPR_{789} would acquire in thermal equilibrium at the inferred gas temperatures T_{86} and T_{97} .

Whereas the results presented by N19 for HH7 showed a steady increase of OPR_{678} from a value of ~ 0.5 at the red edge to ~ 2 at the blue edge, in the sources studied in the present paper there is no strong evidence for a systematic variation of the OPR with LSR velocity. This negative result, of course, is equivalent to the finding (noted in Section 3) that any velocity shifts between ortho- and para- H_2 are small. There are, however, systematic differences between T_{86} and T_{97} and between OPR_{678} and OPR_{789} (with the sense that $T_{86} < T_{97}$ and

$\text{OPR}_{678} < \text{OPR}_{789}$). These are both a natural consequence of the positively curved rotational diagram that can result when there is a mixture of gas temperatures along the sightline. Because the definition of OPR_{XYZ} (see above) is based on a *linear* interpolation of the rotational diagram between the $J = X$ and $J = Z$ states, the effect of positive curvature will tend to overestimate the OPR when Y is even (i.e., when $J = Y$ is a para-state) and underestimate the OPR when Y is odd. We therefore expect the actual OPR in the hot gas to be bracketed by OPR_{678} and OPR_{789} .

Several factors may contribute to the absence of detectable ortho–para velocity shifts in these sources. In the case of IC 443C, which was selected as a control against which the other sources were to be compared with EXES, previous Spitzer/IRS observations of the H_2 S(0)–S(7) lines (D. A. Neufeld et al. 2007) had revealed no significant

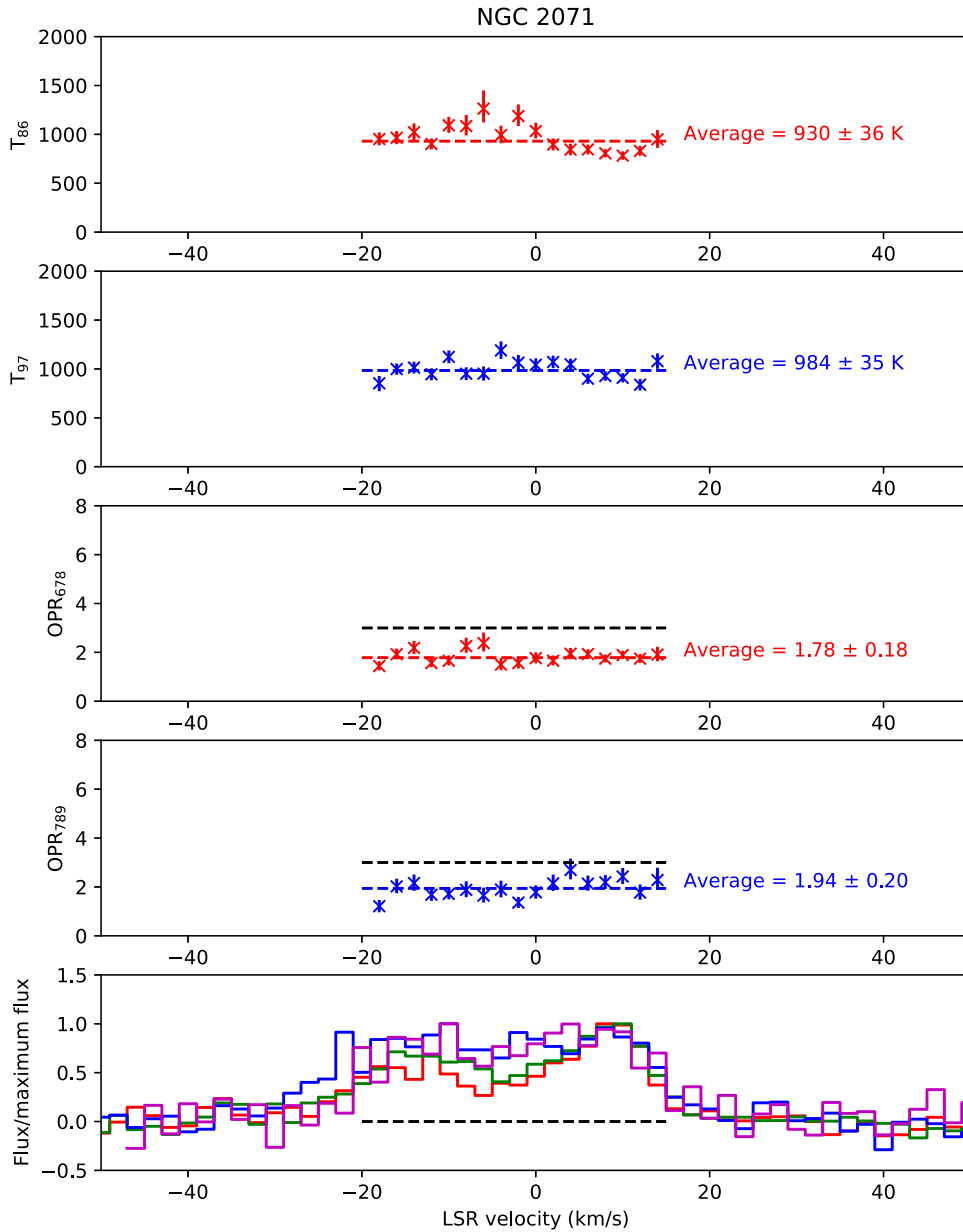


Figure 8. Results obtained for NGC 2071. Top two panels: T_{XY} , the temperature derived from the relative populations in the $\text{H}_2 J = X$ and Y states. Next two panels: OPR_{XYZ} , the ortho-to-para ratio derived from the relative populations in the $\text{H}_2 J = X, Y,$ and Z states. Bottom panels: scaled spectra, rebinned to 2 km s^{-1} resolution, with the same color coding as in Figures 4–6.

departures from an OPR of 3. In this source, the shock is likely propagating in material that *already* possesses an OPR close to the high-temperature equilibrium value of 3. Ortho-to-para conversion occurs only slowly within the cold preshock gas; thus, if the material suffers repeated heating events in shocks that drive the OPR toward its high-temperature equilibrium value, then there may be insufficient time to reset the OPR to a low-temperature value. This possibility is supported by HI (J.-J. Lee et al. 2008) and optical (D. G. York et al. 2000) observations of IC 443 that show filamentary structures lying further from the center of the SNR than clump C, suggesting that the molecular shell to which IC 443C belongs has already been processed by shocks.

For NGC 2071 and 3C 391, by contrast, the lowest J states observed with Spitzer imply the presence of a warm gas component with an OPR significantly below the LTE value.

The H_2 line fluxes in these sources (D. A. Neufeld et al. 2009; T. Giannini et al. 2011) are well accounted for by a two-component model that invokes a warm (250–350 K) gas component responsible for the lower-lying transitions and a hot (1000–1100 K) component responsible for the higher-lying transitions: such models yield best estimates of 0.52 and 0.65 for the OPR in the warm components in NGC 2071 and 3C 391, respectively. Although not as extreme as the value of 0.21 obtained for the warm component in HH7 (D. A. Neufeld et al. 2007), these values imply the presence of preshock gas with a low-temperature OPR. As was widely observed in Spitzer observations of shocked regions (e.g., D. A. Neufeld et al. 2006, 2007, 2009), the hot gas component in these sources, primarily traced by the $\text{H}_2 \text{S}(4)\text{--}\text{S}(7)$ lines, exhibits a larger OPR than the warm component. This behavior likely reflects the fact (D. A. Neufeld et al. 2006) that para-to-ortho

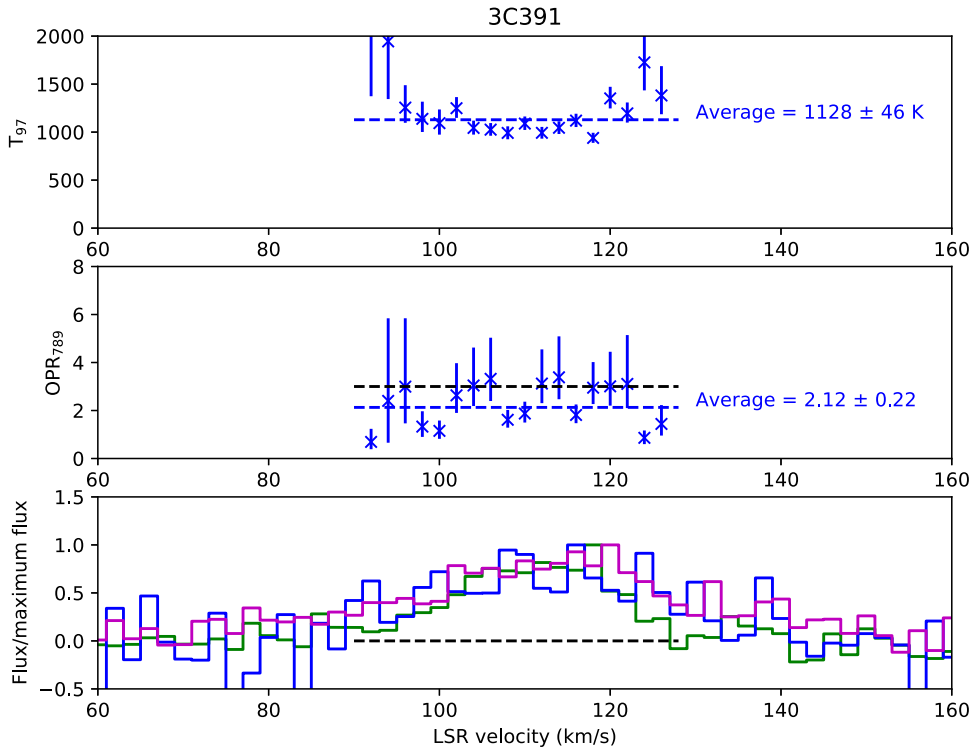


Figure 9. Results obtained for 3C 391. Top panel: T_{97} , the temperature derived from the relative populations in the H_2 $J = 7$ and 9 states. Middle panel: OPR_{789} , the ortho-to-para ratio derived from the relative populations in the H_2 $J = 7, 8$, and 9 states. Bottom panels: scaled spectra, rebinned to 2 km s^{-1} resolution, with the same color coding as in Figures 4–6.

conversion proceeds primarily through reactive collisions with atomic hydrogen that possess a significant activation energy barrier ($E_A/k \sim 3900 \text{ K}$). In this picture, multiple shocks with different velocities are present within the beam, with the lower velocity shocks leading to lower temperature gas within which the timescale for complete para-to-ortho conversion exceeds the period for which the gas remains warm.

Because NGC 2071 and 3C 391 both possess a warm gas component with an OPR far below the equilibrium value, we had expected them to be excellent targets for the detection of ortho–para velocity shifts like those observed previously in HH7. The absence of such shifts in the SOFIA data reported here may reflect the presence of a different geometry than that in HH7. The shocked gas in NGC 2071 and 3C 391 lacks the well-defined bow shock morphology apparent in HH7, raising the possibility that multiple shocks with different propagation directions are present within the slit, or along the line of sight, and contribute to the S(4)–S(7) line emissions. This possibility also becomes more likely because the projected apertures are considerably larger than in HH7, owing to the greater source distances (estimated as 0.39 and 9 kpc, respectively, for NGC 2071 and 3C 391, as compared to 0.22 kpc for HH7); observations at higher spatial resolution (but poorer spectral resolution) with JWST would be complementary here and could reveal structures on scales smaller than the EXES slit size.

Although detailed calculations will be presented in a future study (W. T. Reach et al. 2024, in preparation), any model in which the broad observed lines are attributed to velocity gradients within a single shock is expected to show an ortho–para shift if the initial OPR is low enough, regardless of whether it invokes C- or CJ-type shocks and whether the model is stationary or nonstationary. The one exception here might be

a hot and partially dissociative shock in which the high temperature resets the OPR *before* the bulk of the H_2 emission occurs.

Acknowledgments

Based on observations made with the NASA/DLR Stratospheric Observatory for Infrared Astronomy (SOFIA). SOFIA was jointly operated by the Universities Space Research Association, Inc. (USRA), under NASA contract NAS2-97001, and the Deutsches SOFIA Institut (DSI) under DLR contract 50 OK 0901 to the University of Stuttgart. D.A.N gratefully acknowledges the support of a SOFIA/USRA grant, SOF09-0021; W.T.R. that of SOFIA/USRA grant 07-0007; and S.C., A.G., and P.L. that of the Programme National “Physique et Chimie du Milieu Interstellaire” (PCMI) of CNRS/INSU with INC/INP co-funded by CEA and CNES. We are grateful to the EXES PI, Matt Richter, and the EXES team for their support of the observations presented here.

ORCID iDs

David A. Neufeld <https://orcid.org/0000-0001-8341-1646>
William T. Reach <https://orcid.org/0000-0001-8362-4094>

References

- Chernoff, D. F., Hollenbach, D. J., & McKee, C. F. 1982, *ApJL*, **259**, L97
Clarke, M., Vacca, W. D., & Shuping, R. Y. 2015, in *ASP Conf. Ser.* 495, *Astronomical Data Analysis Software and Systems XXIV (ADASS XXIV)*, ed. A. R. Taylor & E. Rosolowsky, 355
Cushing, M. C., Vacca, W. D., & Rayner, J. T. 2004, *PASP*, **116**, 362
Draine, B. T. 1980, *ApJ*, **241**, 1021
Flower, D. R., Pineau des Forets, G., & Hartquist, T. W. 1985, *MNRAS*, **216**, 775
Giannini, T., Nisini, B., Neufeld, D., et al. 2011, *ApJ*, **738**, 80

- Lee, J.-J., Koo, B.-C., Yun, M. S., et al. 2008, [AJ](#), **135**, 796
- Neufeld, D. A., DeWitt, C., Lesaffre, P., et al. 2019, [ApJL](#), **878**, L18
- Neufeld, D. A., Hollenbach, D. J., Kaufman, M. J., et al. 2007, [ApJ](#), **664**, 890
- Neufeld, D. A., Melnick, G. J., Sonnentrucker, P., et al. 2006, [ApJ](#), **649**, 816
- Neufeld, D. A., Nisini, B., Giannini, T., et al. 2009, [ApJ](#), **706**, 170
- Reach, W. T., Tram, L. N., Richter, M., et al. 2019, [ApJ](#), **884**, 81
- Richter, M. J., Dewitt, C. N., McKelvey, M., et al. 2018, [JAI](#), **7**, 1840013
- Roueff, E., Abgrall, H., Czachorowski, P., et al. 2019, [A&A](#), **630**, A58
- York, D. G., Adelman, J., Anderson, J. E., et al. 2000, [AJ](#), **120**, 1579